SANDIA REPORT

SAND97-0258 • UC-~~404~~ 904
Unlimited Release
Printed February 1997

Designed Supramolecular Assemblies for Biosensors and Photoactive Devices LDRD Final Report

X.-Z. Song, J. A. Shelnutt, J. D. Hobbs, J. Cesarano

Prepared by
Sandia National Laboratories
Albuquerque, New Mexico 87185 and Livermore, California 94550

Sandia is a multiprogram laboratory operated by Sandia Corporation, a Lockheed Martin Company, for the United States Department of Energy under Contract DE-AC04-94AL85000.

Sandia National Laboratories

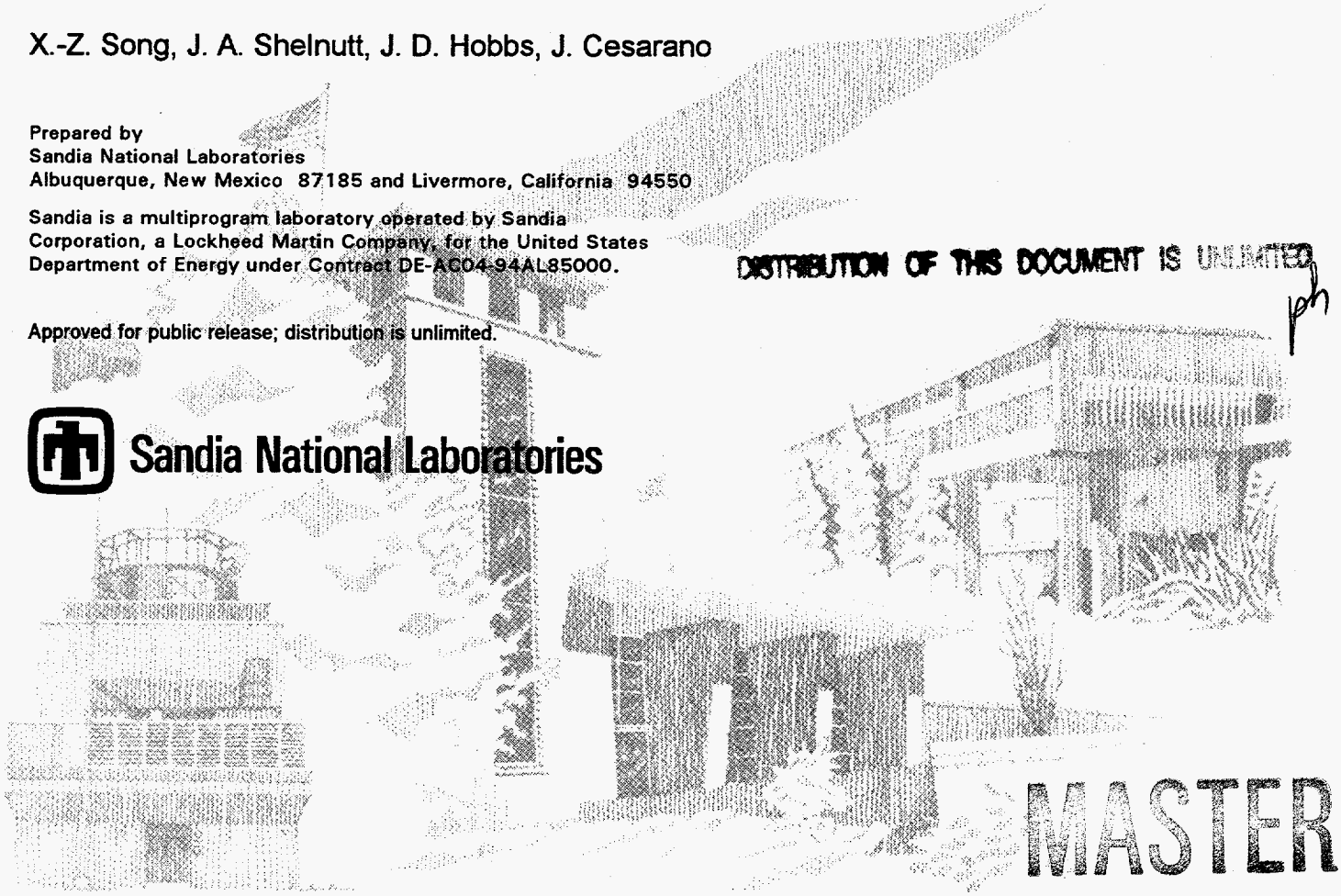

SAND97-0258
Unlimited Release
Printed February 1997

Distribution
Category UC-~~404~~ 904

Designed Supramolecular Assemblies for Biosensors and Photoactive Devices

LDRD Final Report

X.-Z. Song, J. A. Shelnutt (6211), J. D. Hobbs (9225), J. Cesarano (1831)
Fuel Science, Computational Materials Science, and Direct Fabrication Departments

Sandia National Laboratories
P. O. Box 5800
Albuquerque, NM 87185-0710

Abstract

The objective of this project is the development of a new class of supramolecular assemblies for applications in biosensors and biodevices. The supramolecular assemblies are based on membranes and Langmuir-Blodgett (LB) films composed of naturally-occurring or synthetic lipids, which contain electrically and/or photochemically active components. The LB films are deposited onto electrically-active materials (metal, semiconductors). The active components film components (lipo-porphyrins) at the surface function as molecular recognition sites for sensing proteins and other biomolecules, and the porphyrins and other components (*e.g.*, fullerenes) incorporated into the films serve as photocatalysts and vectorial electron-transport agents. Computer-aided molecular design (CAMD) methods are used to tailor the structure of these film components to optimize function. Molecular modeling is also used to predict the location, orientation, and motion of these molecular components within the films. The result is a variety of extended, self-assembled molecular structures that serve as devices for sensing proteins and biochemicals or as other bioelectronic devices.

Table of Contents

List of Figures

List of Tables

Introduction.

The objective of this project is the development of a new class of supramolecular assemblies for applications as biosensors and other biodevices. The supramolecular assemblies are based on membranes and Langmuir-Blodgett (LB) films composed of naturally-occurring or synthetic lipids, which contain electrically and/or photochemically active recognition sites. Depending on the transduction mode, the supramolecular assemblies are in the form of membranes, micellar systems, and thin films on electrically-active substrates. We have improved our biosensor designs and designed the lipoporphyrins (Figure 1a-d) with special structural and photo-chemical properties as the recognition site for the target molecules (paraquat, cytochromes *c*). These structural features include: (1) solvent accessibility of the porphyrin head group at Langmuir-Blodgett (LB) film, (2) isolation of the lipoporphyrin molecules in the lipid phase of the LB film, (3) selective binding of a target molecule (molecular recognition), such as cytochrome *c* or paraquat, and (4) binding-specific photochemical or photo-electro-chemical activity (transduction). We have synthesized the lipoporphyrin 1b and 1c, shown in Figure 1. These lipoporphyrins (LipoPOME) have been shown to possess all of the major structural features required of the biosensor that we have initially selected for construction, except possibly high selectivity of the molecular recognition site for the target molecules. With these lipoporphyrins, which differ only slightly from lipoporphyrin **1a** (LipoP), we have been able to complete most of our goals toward the construction of the desired biodevice. The procedures for preparation of the desired LB films were developed for LipoPOME, which were shown to give films with most of the desired properties. The designed recognition and photochemical properties were tested and confirmed for the target molecule, paraquat, using ternary electron-transfer systems. The tests were performed in micelles and at water-hexane interfaces to mimic the environment of electron

transfer between aqueous solvent and organic lipid phase of LB film. The electron transfer mechanism and kinetic behavior have been studied. Progress on each task will now be described in detail.

Accomplishments.

1. Synthesis of lipoporphyrins (1b) with a molecular recognition site for cytochrome c and paraquat.

The first step in the development of the desired biosensor is to design and synthesize a detergent molecule with long aliphatic tails and a hydrophilic porphyrin head group which will then be incorporated into a lipid monolayer. In the LB film, the porphyrin will serve as a photoelectrochemical agent and also as a molecular-recognition site for binding the molecules to be sensed by the biodevice. Molecular modeling was used to design a number of possible lipoporphyrins and several promising lipoporphyrins were selected for the purpose of selectively binding the protein cytochrome *c* (protein sensor) and, alternatively, the small molecule methylviologen (herbicide sensor: paraquat). The design methodology relies upon both an understanding of the synthetic strategies currently available and the reliable prediction of molecular structures provided by the molecular mechanics models developed in prior work.

Synthesis of nickel(II) 2,3,7,8,12,13,17,18-octa(aceticacid-methylester)-5,10,15,20-tetra(phenyl-eicosanate)porphyrin (NiLipoP). All reagents and solvents were purchased from Aldrich unless otherwise noted. The anhydrous solvents used were packaged in Sureseal bottles.

Eicosanyl-4-formylbenzoate. 4-Carboxybenzaldehyde (500 mg, 3.3 mmol) was esterified by treatment with carbonyldiimidazole (1.3 g, 8.0 mmol) in dry THF (50 mL) at reflux overnight. 1-Eicosanol (5.0 g, 16.7 mmol) and sodium metal (2 mg, 0.1 mmol) were added to the solution at room temperature. After 1 hr an aliquot was quenched with water and extracted with hexane. The organic layer showed one fluorescent product by TLC (SiO_2, R_f 0.4 in 30% CH_2Cl_2/hexane). The rest of the reaction was worked up by extraction of the product in CH_2Cl_2 and hexane,

washing three times with water, drying over anhydrous Na_2SO_4 and removal of solvents. The desired benzaldehyde was purified using flash chromatography (silica, 50% petroleum ether/CH_2Cl_2), yielding 376 mg (28% un-optimized yield). MP 61°C; NMR: ($CDCl_3$), 10.03 (s, 1H, CHO); 8.18 (d, 2H, ArH); 7.93 (d, 2H, ArH); 4.33 (t, 2H, OCH_3); 1.75 (t of t, 2H, $C\underline{H}_2CH_2O$); 1.41 (t of t, 2H, $C\underline{H}_2CH_2CH_2O$); 1.4-1.0 (m, 32H, $(CH_2)_{16}$); 0.85 (t, 3H, CH_3). MS(FAB): 431 m/Z $[M+H]^+$.

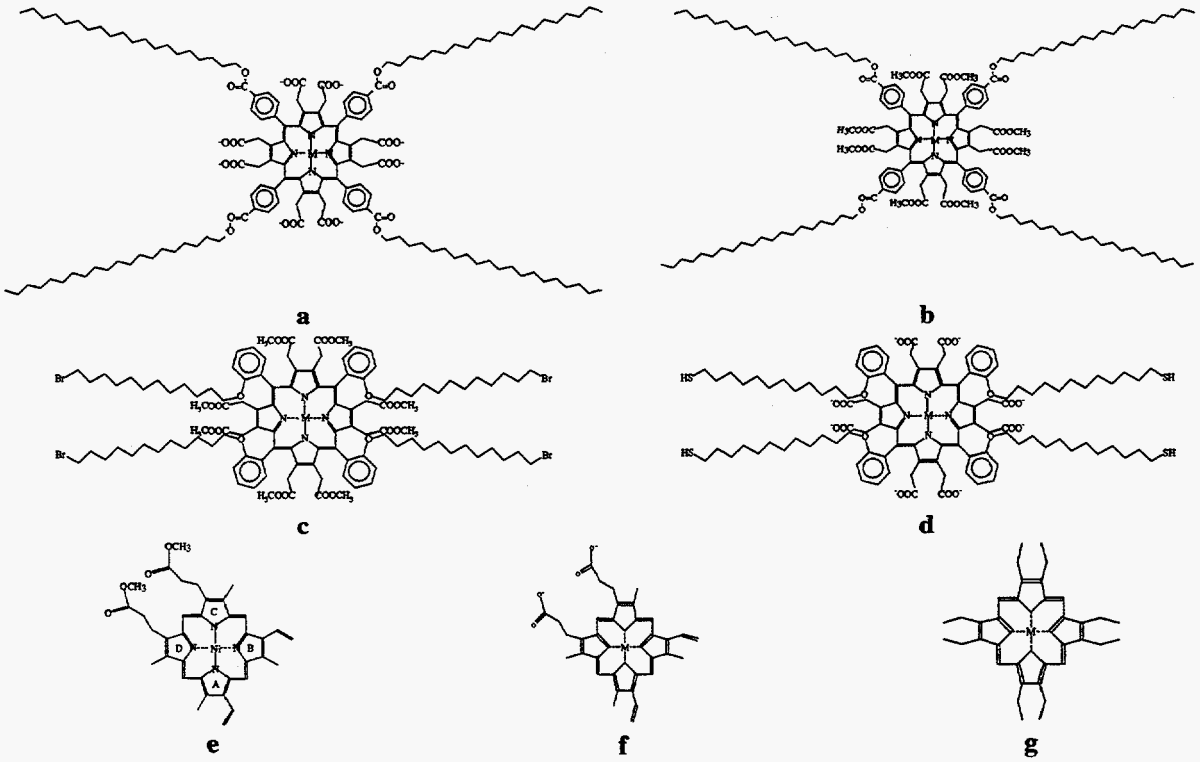

Figure 1. **(a)** *Metal octaacetic-acid-*meso-*tetraphenylporphyrin tetraeicosanate,* **(b)**. *the octamethylester form of* **a**, **(c)** *metal octaacetic-acid-*meso-*tetra(phenyldecanylbromide-ether)porphyrin,* **(d)** *the thiol free-acid forme of* **c**, **(e)** *Ni(II) proto-porphyrin IX dimethyl-ester (NiPPDME),* **(f)** *metal proto-porphyrin (MPP), and* **(g)** *metal octaethylporphyrin (MOEP).*

Nickel(II) octaacetic acid tetrakis(4-eicosanyloxycarbonylphenyl)porphyrin octamethylester. Diacetic acid pyrrole dimethylester (52 mg, 0.25 mmol) and eicosanyl-4-

formylbenzoate (106 mg, 0.25 mmol) were dissolved in dry CH_2Cl_2 (15 mL) and N_2 was bubbled in for 20 min with stirring. 2.5 M BF_3·etherate (10 μL) was added and the solution was allowed to stir in the dark at room temperature for 1.5 hr. The progress was monitored by optical spectroscopy by oxidizing a small aliquot of the porphyrinogen solution to porphyrin with dichlorodicyanobenzoquinone (DDQ). DDQ (56 mg, 0.25 mmol) was added and the solution was allowed to reflux for 30 min. The solvents were removed *in vacuo* and nickel was inserted into the porphyrin without further purification.

The residue in chloroform (10 mL) was treated with a saturated solution of nickel(II) acetate in methanol (4 mL) and glacial acetic acid (2 drops) at reflux for 1 hr. At this time, the absorption spectrum showed only the metalloporphyrin so the solution was cooled and worked up by extraction by CH_2Cl_2 as described above. The desired porphyrin was isolated using preparative TLC (silica, 2% acetone/CH_2Cl_2). The fast-running red band was collected and dried yielding 23 mg of product. NMR ($CDCl_3$): 8.30 (d, 8H, ArH); 8.03 (d, 8H, ArH); 4.43 (t, 8H, CH_2O); 3.33 (s, 24H, CH_3O); 3.22 (s, 16H, CH_2CO_2); 1.86 (t, 8H, $C\underline{H}_2CH_2O$); 1.22 (m, 136H, $(CH_2)_{17}$); 0.84 (t, 12H, CH_3); UV/vis(CH_2Cl_2): 441, 558, 588(sh). MS(FAB): 2545 (m/Z [M^-]).

Zinc (II) octaacetic acid tetrakis-4-eicosanyloxycarbonylphenylporphyrin octamethyl-ester. The same procedure was used as in the nickel derivative except that a saturated methanolic solution of zinc acetate was used instead of nickel acetate. Half the amount of pyrrole and benzaldehyde used for the nickel porphyrin gave 25 mg of the zinc derivative. NMR ($CDCl_3$): 8.35 (d, 8H, ArH); 8.26 (d, 8H, ArH); 4.47 (t, 8H, CH_2O); 3.30 (s, 40H, CH_3O, CH_2CO_2); 1.88 (t of t, 8H, $C\underline{H}_2CH_2O$); 1.51 (t of t, 8H, $C\underline{H}_2CH_2CH_2O$); 1.4-1.2 (m, 128H, $(CH_2)_{16}$); 0.85 (t, 12H, CH_3); UV/vis(CH_2Cl_2): 464, 596, 654(sh).

Tin (IV) octaacetic acid tetrakis-4-eicosanyloxycarbonylphenylporphyrin octamethylester. The previously described procedure was used to synthesize the lipoporphyrin diacid. Instead of using the crude reaction mixture for the metal insertion, however, the porphyrin was first purified by preparative TLC (silica, 5% acetone/CH_2Cl_2). The porphyrin diacid was treated with anhydrous $SnCl_2$ and dry pyridine (5 mL) at reflux for 2 hr. The optical spectrum showed only metalloporphyrin so the reaction was allowed to cool and then worked up by extraction with CH_2Cl_2. The tin porphyrin was then purified using preparative TLC (silica and 10% [1% formic acid/acetone] in CH_2Cl_2). The major green band (Rf ≈0.5) was isolated and confirmed by optical and NMR spectroscopies to be the desired porphyrin. NMR ($CDCl_3$): 8.42 (d, 8H, ArH); 8.37 (d, 8H, ArH); 4.49 (t, 8H, CH_2O); 3.22 (s, 24H, OCH_3); 1.91 (t of t, 8H, $C\underline{H}_2CH_2O$); 1.55 (t of t, 8H, $C\underline{H}_2CH_2CH_2O$); 1.5-1.1 (m, 128H, $(CH_2)_{16}$); 0.85 (t, 12H, CH_3). UV/vis: (CH_2Cl_2) 457, 592, 641.

2. Preparation of LB films with incorporated lipoporphyrins designed to recognize cytochrome *c*.

LB films of NiLipoPOME and, for comparison, Ni protoporphyrin IX dimethylester (NiPPDME, , Fig. 1e) were prepared on glass slides and silicon wafers using a Langmuir trough as follows. LB films of NiLipoP were prepared on glass slides (Fisher Microscope Slides) using a NIMA Model 2011 Langmuir trough. Glass slides were washed in detergent and sonicated in a bath sonicator (ultrasonic cleaner, Branson Ultrasonics). After washing the glass slides in deionized water, they were cleaned by heating (70 °C) in a mixture of 30% H_2O_2 and concentrated H_2SO_4 (30:70 v/v) for 30 min. After thoroughly rinsing with deionized water, the glass slides were stored under water until silanation. The water was purified by using a Millipore

reverse osmosis/ion-exchange system.

All the silanation reactions were performed in a glovebox under a dry nitrogen atmosphere. Octadecyltrichlorosilane (OTS) was purchased from Sigma. The silanation solution was prepared by adding 30 mL dodecane and 2 μL OTS to a 30-mL solution of water-saturated chlorinated solvents prepared by decanting two volumes of $CHCl_3$ and three volumes of CCl_4 under a layer of water overnight and drawing the water layer away by a pump before use. Silanations were performed at 18 °C in an ultrasonic bath (MGW LAUDA RM6, Brinkmann) for 15 min. After reaction, treated glass slides were thoroughly rinsed with chloroform and heptane and stored under heptane before deposition.

Solutions of $2x10^{-4}$ M cadmium chloride in water were used as the subphase (pH=6.2). The spreading solution was a 10^{-4} M solution of lipoporphyrin mixed with stearic acid (molar ratios 1:30, 1:15, or pure) in chloroform.

The isotherms were measured at room temperature with compression speeds of 250 or 50 cm^2/min. Two condensed phases were observed above and below a plateau in the isotherms at about 18 mN/m. Consequently, two types of LB films were produced: a low pressure film for which the surface pressure held at 14 mN/m during deposition and a high pressure film for which the pressure was maintained at 27 mN/m. The vertical dipping method was used. Up to 20 layers (Y-type deposition) were deposited onto the substrates at a speed 4 mm/min for the first layer, 2 mm/min for the second, and 20 mm/min for the rest of the layers. For comparison, mixed stearic acid-nickel(II) protoporphyrin IX dimethylester (NiPPDME-SA) LB films were prepared on glass substrates under similar conditions (except that the pressure was maintained at 28 mN/m).

3. Structural studies of LB films containing lipoporphyrins.

The Π-A isotherms for mixed NiPPDME-SA and mixed NiLipoP-SA Langmuir monolayers are shown in Figure 2. For the NiPPDME-SA monolayer, there is a plateau in the isotherm at 47 mN/m (Π_c). The plateau most likely results from the porphyrin molecules being gradually squeezed out of the crystalline lipid monolayer. This is described as a gradual collapse (escape of one component into the third dimension), since the pressure does not decrease dramatically. At pressures above 60 mN/m, a catastrophic collapse (decrease in area with a precipitous decrease in pressure, not shown in Figure 2a) is observed as the crystalline lipid monolayer is disrupted due to mechanical instability.

For the NiLipoP-SA (1:30) monolayer, a plateau occurs at 18 mN/m (Π_S). The plateau indicates that the structure of the monolayer film at the air-water interface changes continuously. The NiLipoP-SA isotherm behavior is similar to that observed for several mixed lipid-dye monolayers, such as the monolayer composed of zinc tetra-*m*-eicosylpyridium porphyrin bromide and L-α-dimyristoyl-phosphatidylethanolamine (DMPE) observed by Flörsheimer and Möhwald, for which the plateau near 20 mN/m was described as a fluid-gel phase transition in which the porphyrin separates into the fluid lipid phase. Above 35 mN/m, catastrophic collapse of the monolayer occurs.

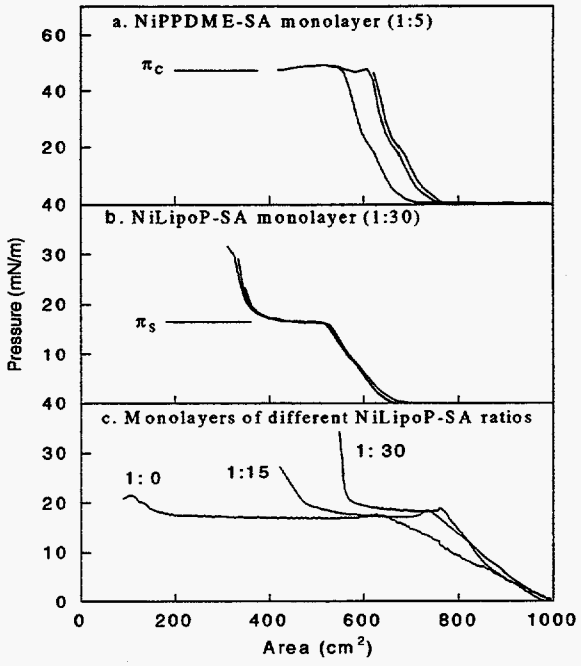

Figure 2. *Pressure-area isotherms of NiPPDME-stearic acid (a), NiLipoP-lipid (b), and different ratio NiLipoP-lipid (c).*

Pressure-area isotherms for NiPPDME-stearic acid LB films. For NiPPDME, the phase change corresponding to Π_c could be caused either by an irreversible change in the orientation of the porphyrin ring in the film, for example, from "horizontal" to "vertical" packing, or by irreversible precipitation of porphyrin from the lipid monolayer as 3-dimensional clusters. For monolayers of pure simple esterified porphyrins such as mesoporphyrins and protoporphyrins (porphyrins without long alkyl chains), it has been suggested on the basis of molecular areas that the ester groups are sufficiently polar to orient the porphyrin in the monolayer, resulting in approximately vertical packing of the rings with the two ester groups in contact with the water surface. We also expect a vertical orientation for NiPPDME in our mixed stearic acid monolayers, thus a change from horizontal to vertical packing cannot be the cause of the plateau at Π_c.

It is known that most porphyrins like NiPPDME do not form homogeneous monolayers with lipids, but aggregate to form clusters that are squeezed out of the lipid monolayer at high pressure. Aggregation of the porphyrin in mixed monolayers can be controlled to some extent by maintaining low surface pressure, as well as by the addition of divalent counterions to the subphase. However, a high degree of aggregation of NiPPDME occurs when surface pressure is high. At pressures above Π_c, the aggregated clusters are large enough to see easily with the unaided eye as colored particles of porphyrin floating on the air-water interface. Moreover, repeated compression-expansion-recompression isotherms show that there is little decrease in the area in the repeated recompression isotherms if the barriers are opened before Π_c is reached, indicating that not much precipitation occurs at pressures below Π_c. In contrast, when the barriers are opened after Π_c is reached, the area in recompression isotherms irreversibly decreases

as the porphyrin crystallites are squeezed out of the monolayers. When the barriers are opened after reaching pressures significantly higher than Π_c, there is no plateau observed in the recompression isotherm because all of the NiPPDME is in the form of crystallites, and only lipid remains in the monolayer. (There may also be some degree of lipid membrane collapse accompanying the precipitation.) The low solubility of NiPPDME in the crystalline lipid phase provides the driving force for π–π aggregation of NiPPDME first, followed by porphyrin crystallite formation. Consequently, we could only obtain LB films at deposition pressures lower than Π_c (low pressure film).

Pressure-area isotherms for NiLipoP-stearic acid LB films. NiLipoP has a polar head group composed of the porphyrin macrocycle surrounded by the twelve polar ester groups. The four hydrophobic tails consist of twenty-carbon linear alkanes attached to the *meso*-phenyl rings through ester bonds. We have previously shown that the strong nonplanar distortion of the porphyrin macrocycle and the steric bulk of the twelve ester substituent groups effectively preclude π–π aggregation of the porphyrin head groups. Others have found that long alkyl tails attached to the porphyrins help to prevent phase separation from the lipid monolayer and allow formation of more homogeneous monolayers. Indeed, visual inspection of the NiLipoP films does not detect any NiLipoP crystallites at pressures well above Π_S (18 mN/m). Also, repeated compression-expansion-recompression isotherms (Figure 2b) do not show a significant irreversible decrease in the area when the barriers are opened at pressures greater than Π_S, consistent with the lack of 3-dimensional cluster formation. The steep slope above Π_S is characteristic of a solid phase, and the less steep slope below Π_S is characteristic of a liquid (fluid) phase (Figure 2b). To further characterize the structure of the monolayer above and below the

plateau, we transferred multiple monolayers onto substrates at both high (27 mN/m) and low (14 mN/m) surface pressures (*vide infra*).

The pressure-area isotherms of NiLipoP with different molar ratios of SA are shown in Figure 2c. A plateau at approximately the same pressure (17 mN/m) as Π_S also appears in the Π-A isotherm of the pure NiLipoP monolayer (1:0 monolayer). For the pure NiLipoP monolayer, the area extrapolated to zero surface pressure (limiting area) for the low pressure region is 420 $Å^2$/NiLipoP, which is larger than the calculated area occupied by one lipoporphyrin head group lying parallel to the surface (360 $Å^2$/NiLipoP). The limiting area is larger because of the disorder in the packing of the porphyrin in the liquid phase. The extrapolated limiting area for the high pressure region is approximately 180 $Å^2$/NiLipoP. There are two possible structural changes in the films that can account for the isotherm of the pure film. First, it is interesting that the feature appearing just above an area of 100 cm^2 (at high pressures) seems to have a similar slope to that of the isotherm in the region above 600 cm^2 (at low pressures), and also the extrapolated area per NiLipoP (180 $Å^2$) for the high pressure region is half of the calculated area of 360 $Å^2$ occupied by one porphyrin when its head group lies flat on the water surface. Thus, the plateau could result from the porphyrin molecules being gradually pushed out of monolayer to form a bilayer (bilayer model). Another possible cause for the plateau is a change in the orientation of the porphyrin in which the porphyrin becomes more or less perpendicular (edge on) to the surface (orientation change model).

The pure NiLipoP film catastrophically collapses at a pressure slightly higher than Π_S (21 mN/m). For the bilayer model, a porphyrin bilayer collapses; for the orientation-change model, it is a monolayer of edge-on oriented porphyrins that collapses. Furthermore, the catastrophic collapse pressure (21 mN/m) for the pure NiLipoP film is lower than for the collapse pressure of

the 1:15 mixed NiLipoP-SA monolayer, and much lower than the catastrophic collapse pressure of the 1:30 mixed monolayer (35 mN/m). Also, the slopes above the plateau becomes steeper relative to the slope below the plateau for the monolayers with more lipid. Thus, for the NiLipoP-SA monolayers with the most lipid, the structure is more crystalline above the plateau and stable to greater pressures. These observations are difficult to rationalize based on either the bilayer model or the orientation-change model as discussed below. This also suggests that a different structural change may account for the phase transition at Π_S, although we cannot rule out the bilayer model or the orientation models conclusively.

4. Model molecular structure and dynamical motions of the NiLipoP-stearic acid films.

Molecular mechanics calculations suggest that a change in the position of the porphyrin head groups relative to the plane formed by stearic acid head groups in the film may account for the plateau in the isotherms of the mixed Langmuir films and differences in the LB films obtained at pressures above and below Π_S. An energy minimized monolayer is illustrated in Figure 3. Periodic boundary conditions were imposed on the unit cell shown (for clarity, 88 water molecules included in the calculation are not shown). The energy-optimization calculations indicate that the NiLipoP head group energetically favors a position below the average plane of the carboxylic acid moieties of the lipid monolayer as illustrated in Figure 4b and is surrounded by water molecules (not shown). Furthermore, the space underneath the porphyrin head group in Figure 3 (above, in Figure 4b) holds about 12 stearic acid molecules in addition to the 4 eicosanate chains. And, from the geometry of the molecular model, the porphyrin occupies an approximate area of (19Å×19Å ≅) 360 $Å^2$. Thus, both the molecular modeling calculation and the

slope of the Π–A isotherm suggest that the low pressure monolayer and LB films correspond to case (a) of Figure 4 in which the porphyrin and stearic acid are *liquid* and the head groups of the stearic acid molecules and porphyrin are in contact, but the tails are disordered. The porphyrin molecules occupy a larger area than expected on the basis of its size in this loosely packed film (420 Å^2). For the high pressure monolayer and LB films, case (b), the porphyrin tails and the stearic acid molecules are in the *crystalline* phase with their tail groups closely packed as shown in Figure 3.

Interpretation of Pressure-Area Isotherms. For the low pressure mixed films, the total surface areas of the monolayers, calculated using the extrapolated limiting area of 420 Å^2 for one NiLipoP molecule in the pure porphyrin monolayer and an area of 24 Å^2 for SA in the liquid phase, are 985 and 923 cm^2 for the

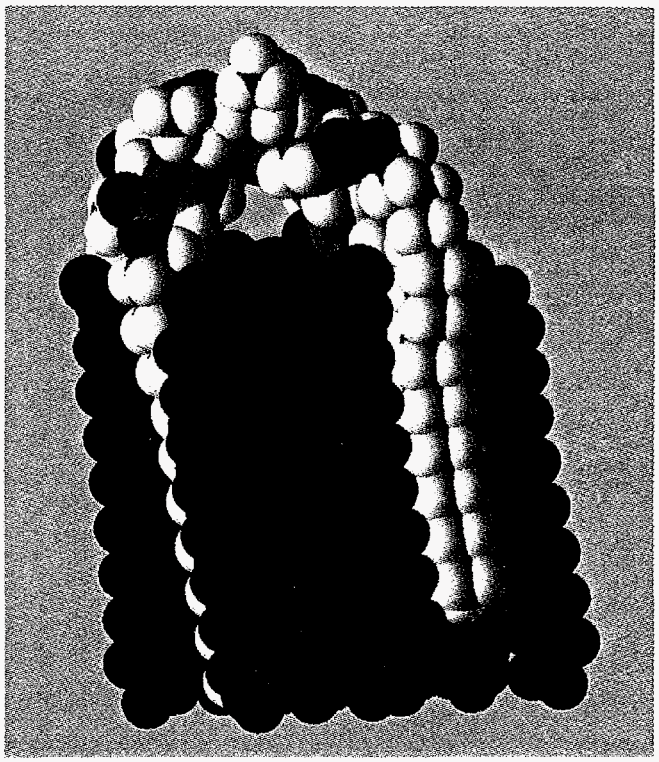

Figure 3. *Energy optimized structure of NiLipoP in stearic acid monolayer at surface pressures above Π_c.*

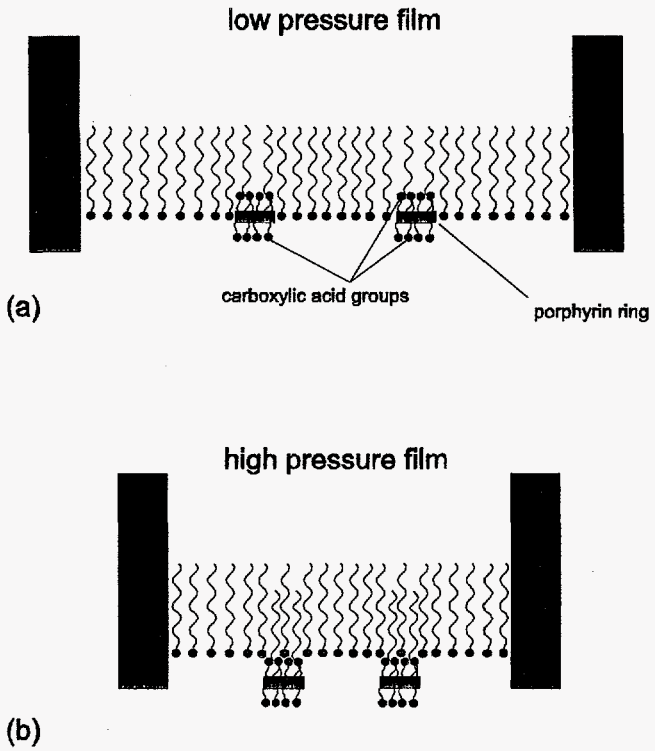

Figure 4. *Schematic representation of NiLipoP-lipid monolayer at surface pressures lower than Π_c (bottom) and at surface pressures higher than Π_c (top).*

1:15 and 1:30 films, respectively. These areas agree well with the experimental film areas of 980 and 920 cm^2, respectively. Thus, neither filling in, nor gradual bilayer formation, nor a change in the orientation of the porphyrin is required to account for the experimental film areas. Further, the areas suggest that the porphyrin lies parallel to the surface.

For the high pressure mixed films, the areas of the monolayers can be calculated using each of the three structural models proposed. For the lipid-fill-in model, the area of the monolayer is the area of the NiLipoP molecules lying parallel to the surface (360 $Å^2$/molecule) plus the area of the lipid molecules, excluding the area of the 12 underlying stearic acid molecules per porphyrin molecule that do not contribute to the total monolayer area. For the orientation-change model, the area of the monolayer is the area of the NiLipoP molecules in the high pressure, pure porphyrin film (180 $Å^2$/molecule) plus the area of all of the lipid molecules. For the bilayer model, we assume that the porphyrin and SA molecules are phase separated into domains. In the porphyrin domain, the area of the bilayer is the area of half of the porphyrin molecules (each porphyrin molecule occupies an area of 360 $Å^2$). In the lipid domain, the area is just the area of all of the lipid molecules, as for the orientation change model. For all three models the area of the SA molecules is assumed to be 21 $Å^2$, the area of a stearic acid molecule in the solid phase of a pure SA monolayer. With these assumed areas, the total surface areas for the mixed NiLipoP-SA monolayers with ratios of 1:15 and 1:30 are calculated and listed in Table 1. One might also have to consider a model for which all the porphyrin is squeezed out of the SA monolayer, but the areas for such a model are in poor agreement with the experimentally determined areas.

The fill-in model gives the best agreement with the experimental area for the 1:30 high pressure film, but poorer agreement with the 1:15 film. Because there are barely enough SA

molecules to fill in under the porphyrin, packing disorder or a porphyrin orientation change might be expected for the 1:15 ratio films. Our lipid-fill-in model is almost identical to a model proposed by Möbius *et al.* to account for the behavior of a mixed monolayer of a lipoporphyrin, tetra-*m*-octadecanoylpyrridiumporphine, with arachidic acid and methylarachidate (molar ratio 1:10:10). They found that the transition moments of the porphyrin macrocycle are oriented parallel to the surface, and further proposed that the accessible space on top of the flat chromophore is filled-in with matrix molecules, resulting in a densely packed matrix of hydrophilic chains.

At present we cannot completely rule out the orientation-change and bilayer models as a cause of the plateau at Π_S on the basis of the monolayer area calculations. However, as pointed out above, it is hard to understand the trends with increasing lipid content in the slope above the plateau and in the catastrophic collapse pressure in terms of these models. Summarizing, the lipid fill-in model, suggested by the molecular mechanics calculations, is in favorable agreement with the area reduction observed in the isotherms. On the other hand, the orientation-change and bilayer models find some support in the area reduction implied by the UV-visible spectroscopic evidence.

5. Characterization of the lipoporphyrin and LB films using spectroscopic techniques.

Oriented UV-visible absorption spectroscopy, resonance Raman spectroscopy, and small angle X-ray reflection measurements were used to characterize the LB films. From these studies, information about the structure, position, and orientation of the lipoporphyrin in the films has been determined. X-ray reflection measurements show that the films are well ordered. Further,

modeling of the small angle X-ray data is underway and will provide more detailed infomation about the morphology of the NiLipoPOME-stearic acid films.

UV-visible absorption spectroscopy. The UV-visible absorption data for all of the Ni-porphyrin solutions and LB films are summarized in Table 1. The typical absorption spectra of mixed NiPPDME-lipid monolayers exhibit a red shift of the Soret band by 4-5 nm relative to NiPPDME in methylene chloride solution. There are also red shifts of Q bands and an additional shoulder at about 586 nm. The Soret bands exhibit significant broadening compared with those in solution. These shifts and broadenings are typical of aggregates of metalloporphyrins. The shifts are small, indicating a different structure for the aggregate and possibly a different degree of aggregation for NiPPDME. As expected, the absorbance of the porphyrin is approximately proportional to the number of deposited layers. Also, the full width at half-maximum of spectral bands is constant in films of different numbers of monolayers. These features of the absorption spectra suggest the absence of appreciable interlayer interactions or differences in the environment of the porphyrin from layer to layer.

Table 1. *Wavelengths (nm) of the maxima of the porphyrin absorption bands for metal porphyrins in films and under various solution conditions.*

Porphyrin	Environment	α	β	γ
NiPPDME	CH_2Cl_2	560	523	400
NiPPDME	SA-18 monolayers	563	528	405
NiPPDME	SA-12 monolayers	562	526	404
NiPPDME	SA-6 monolayers	562	526	404
NiPP	CTAB/H_2O	561	522	399
NiPP	H_2O/pH 11	566	530	384
CuPP	CTAB/H_2O	575	535	405
CuPP	H_2O/pH 11	585	550	385
NiLipoP	CH_2Cl_2	558	601	443
NiLipoP	SA-20-14mN/m	560	603	447
NiLipoP	SA-20-27mN/m	560	603	447

NiPP in aqueous CTAB-micellar solution is known to be monomeric. In contrast, NiPP in aqueous solution is known to exist in varying degrees of π–π aggregation depending on the pH; lowering the pH enhances aggregation. The absorption spectra exhibit blue shifts of the Soret bands from 400 to 384 nm and red shifts of Q bands upon aggregation. Either blue or red shifts

may be observed depending on the structure of the aggregate. The Soret band of the solution aggregate has a long wavelength red tail extending to about 500 nm, attributable to exciton coupling in the B band. With the increase in aggregation caused by lowering of the solution pH, the intensity of this tail increases. The absorption spectra of the more planar Cu derivative of protoporphyrin show the same trends in aqueous CTAB micelles and in water solution. The spectral changes observed upon aggregation of metalloprotoporphyrins are generally similar to those observed upon formation of the LB films of NiPPDME, that is, shifts and broadening of the absorption bands are observed.

The absorption spectra of NiLipoP in lipid LB films show that the Soret band is red shifted ca. 4 nm, but does not broaden significantly when compared to spectra of the monomer in solution. The Q bands are red shifted by about 2 nm. Because of the extensive steric crowding of the twelve substituent groups of the porphyrin macrocycle, a highly nonplanar conformation results. The presence of the bulky substituents and the nonplanar conformation together prevent π–π aggregation of the porphyrin head groups. The small red shifts in the absorption spectra are consistent with a change in the solvent environment or a structural change in the porphyrin head group, rather than aggregation of porphyrin chromophores. Furthermore, there are no notable differences in the spectra of the films deposited at different pressures except in the change in magnitude of the absorbance. The ratio of the absorbances for NiLipoP films (1:30 films) deposited at 27 mN/m (above Π_c) to those deposited at 14 mN/m (below Π_c) is 1.4. This area ratio is generally consistent with the area ratio (1.4 *versus* 1.5) obtained from the Π-A isotherms.

Resonance Raman Spectroscopy. Figure 5 shows typical resonance Raman spectra of NiLipoP in methylene chloride, in the low-pressure lipid LB film, and in the high-presssure LB film. There are no significant shifts (<1 cm^{-1}) or changes in relative intensities of the structure-

sensitive marker lines. Three of the structure-sensitive lines at about 1370, 1516 and 1576 cm^{-1} are assigned to the ν_4, ν_3 and ν_2 normal modes of the porphyrin macrocycle. The lack of significant differences in the spectra are consistent with the absence of π–π aggregation in the films and, to some extent, with the lipid fill-in model in that no significant structural changes occur in the porphyrin macrocycle which might be expected for an orientation change.

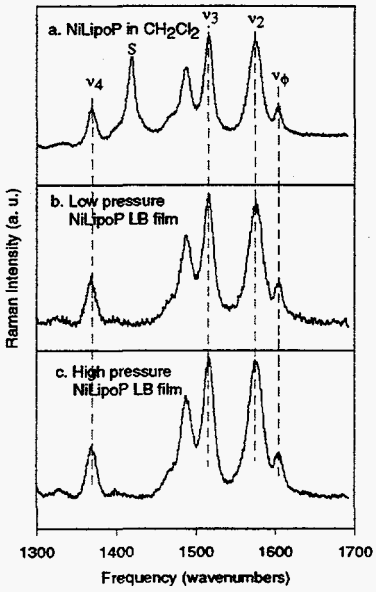

Figure 5. *Resonance Raman spectra of NiLipoP in CH_2Cl_2 (a), in low-pressure mixed lipid film (b), and in high-pressure mixed lipid (c).*

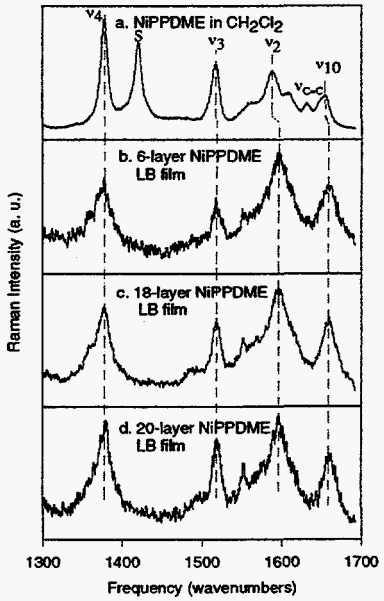

Figure 6. *Resonance Raman spectra of NiPPDME in CH_2Cl_2 (a), in 6-layer (b), 18-layer (c) 20-layer mixed lipid film (d).*

Figure 6 shows typical resonance Raman spectra of mixed NiPPDME-lipid films and NiPPDME in methylene chloride, a non-coordinating solvent. The Raman line frequencies are summarized in Table 2. The following differences are noted between the spectra of the monolayers and the solutions: (a) ν_{10} increases by 4.0 cm^{-1} for the 6-layer film, 5.8 cm^{-1} for the 18-layer film, and 6.2 cm^{-1} for 20 layer film relative to the solution position, (b) ν_2 increases by 8.2 cm^{-1} for the 6-layer film, 7.6 cm^{-1} for the 18-layer film, and 7.4 cm^{-1} for the 20-layer film, (c)

ν_3 increases by 0.6 cm^{-1} for the 6-layer film, 0.8 cm^{-1} for the 18-layer film, and 1.2 cm^{-1} for the 20-layer film, (d) ν_4 remains essentially the same, and (e) the vinyl stretching mode, $\nu_{C=C}$, which appears at 1632 cm^{-1} in methylene chloride solution almost completely disappears.

Table 2. *Frequencies (cm^{-1}) of selected Raman lines for metal porphyrins in films and under various solution conditions.*

Porphyrin	Environment	ν_4	ν_3	ν_2	$\nu_{C=C}$	ν_{10}
NiPPDME	CH_2Cl_2	1377.6	1517.0	1587.8	1631.2	1653.6
NiPPDME	SA-6 monolayer film	1377.8	1517.6	1596		1657.6
NiPPDME	SA-18 monolayer film	1377.6	1517.8	1595.4		1659.4
NiPPDME	SA-20 monolayer film	1378.2	1518.2	1595.2		1659.8
NiPP	CTAB/H_2O	1378.8	1518.8	1591.2	1632	1657.2
	H_2O, pH 9	1379.2	1521.2	1596.2	1630[c]	1659.8
NiPP	CTAB/H_2O	1379	1519	1591.4	1632.2	1657.2
	H_2O, pH 11	1378.8	1519.8	1593.2	1632.2	1657.4
NiPP	CTAB/H_2O	1378.4	1518.6	1590.8	1632.2	1656.8
	H_2O, pH 12	1378.2	1519.2	1593.4	1629.6	1657.2
NiPP	CTAB/H_2O	1378.4	1519	1591.4	1631.8	1657.6
	H_2O, pH 13	1378.4	1518.8	1592.2	~1629	1656.8
CuPP	CTAB/H_2O	1374.2	1500.4	1581.6	~1619	1637
	H_2O, pH 11	1374	1501.4	1580.8	~1619	1637.4
NiPP[a]	CTAB/H_2O	1379	1519	1593	1632	1657
	Cholate/H_2O	1379	1516	1589	1631	1650
NiPP[b]	CTAB/H_2O	1378	1519	1593	~1630	1658
NiHbA[b]	H_2O	1378	1519	1593		1658
NiLipoP	CH_2Cl_2	1370.2	1516	1575.6		
NiLipoP	SA-20 film 14mN/m	1369	1515	1574.8		
NiLipoP	SA-20 film 27mN/m	1369.2	1515.4	1575.6		
NiLipoP	SA/H_2O	1370.8	1516.6	1575.2		
	CH_2Cl_2	1370.8	1516.6	1576.4		
NiLipoP	CTAB/H_2O	1369.4	1516	1574.6		
	CH_2Cl_2	1369.6	1516.4	1576		

These differences for the NiPPDME films compared with solution spectra are consistent with both aggregation and an increase in the planarity of the porphyrin macrocycle. In order to sort out these contributions, we obtained the resonance Raman spectra of monomeric NiPP in CTAB micelles, in which NiPP is an equilibrium mixture of planar and ruffled forms, and aggregated NiPP in water with pH decreasing from 13 to 9, in which the equilibrium between planar and ruffled forms is shifted toward the planar conformer by aggregation. These solution conditions affect the relative concentrations of the planar and nonplanar conformers allowing the

effects of nonplanarity and aggregation to be studied. The upshifts of ν_2, ν_3 and ν_{10} for NiPPDME in the LB films are caused by the change from an equilibrium of planar and ruffled forms in CH_2Cl_2 to solely the planar form in the LB films. Aggregation most likely causes most of this change in the planar-nonplanar equilibrium. The rigid and ordered lipid membrane environment may also be an important factor in forcing the ruffled forms into the planar conformer and possibly modifying the orientation of the vinyl substituents.

The resonance Raman spectra show that NiPPDME exists as a mixture of planar and nonplanar forms in solution. Upon incorporation into lipid monolayers, NiPPDME exists only in the planar form probably because of porphyrin aggregation and the influence of the ordered lipid monolayer environment of the porphyrin. The planar conformation of NiPPDME most likely results from π–π aggregation. Nonetheless, below Π_c the degree of π–π aggregation is low enough to prevent formation of crystallites in these lipid films. Above Π_c, NiPPDME precipitates out of the lipid monolayers.

In contrast, the designed NiLipoP does not display π–π aggregation, precipitation, or significant structural changes upon incorporation into lipid monolayers according to the UV-visible absorption and resonance Raman spectra. The high degree of nonplanarity of the lipoporphyrin macrocycle and the steric constraints of the eight acetic acid methyl ester substituent groups effectively prevent π–π aggregation of the porphyrin head groups in the films. Further, the four long alkyl side chains probably anchor the macrocycle into the lipid monolayer at its surface, prevent porphyrin cluster formation. The lipid fill-in model is consistent with the UV-visible absorption, resonance Raman spectra, and other features in the isotherms.

In conclusion, NiLipoP shows the following desired properties after incorporation into the

LB films: (1) it retains the desired conformation (nonplanar), (2) it protrudes from the film in a favorable location and orientation for binding target molecules, (3) it does not form undesired π–π aggregates. These properties are important for successful applications in chemical sensors and for electron-transport studies.

6. Design improved lipoporphyrins and model structure and dynamics of LB films.

Our goals were to design, synthesize, and characterize improved lipoporphyrin molecular recognition components for the biosensor and to determine if its recognition and photo-electron-transfer properties were suitable for sensing the target herbicide and protein molecules. Because of our success in completing these tasks we are now in a position to simplify the design of the sensor device as shown in Figure 7. Besides simplifying the fabrication of the device, the improvements in the design of the molecular components also are expected to improve performance of the device through improved electron transfer across the film and improved robustness of the device. These enhanced properties result from covalent linkage of the film to the electrode surface and use of only a single monolayer. We designed an improved molecular recognition component with three new features: (1) long aliphatic tails terminated with thiol groups for direct covalent attachment to

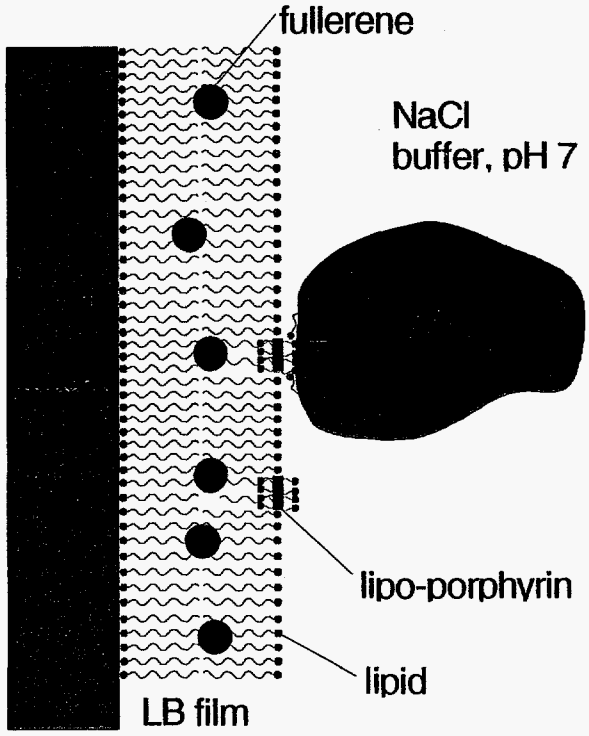

Figure 7a. *The originally designed cytochrome c-specific photo-biosensor*

gold electrodes, (2) the shortened length of the long aliphatic tails (allowing electron transfer directly to the electrode substrate without intermediate fullerene carriers), and (2) a negatively charged hydrophylic porphyrin head group. In the film, this porphyrin will serve as a photoelectrochemical agent (that initiates the electrical current signifying the detection event has occurred) and also as a molecular-recognition site for binding the molecules to be sensed by the device. Molecular modeling was used to design the new lipoporphyrin **1d** with improved properties for selectively binding the target protein cytochrome *c* (protein sensor) and, alternatively, the herbicide paraquat (methylviologen). The design methodology relies upon both an understanding of the synthetic strategies currently available and the reliable prediction of molecular structures and properties provided by the molecular mechanics models developed in previous work. Based on the results of *cytochrome c-spec*the design procedure LipoPOME **1c** with nickel as the metal ion (M=Ni(II)) was selected and synthesized; the ultimate goal of the synthesis is the thiol derivative **1d**.

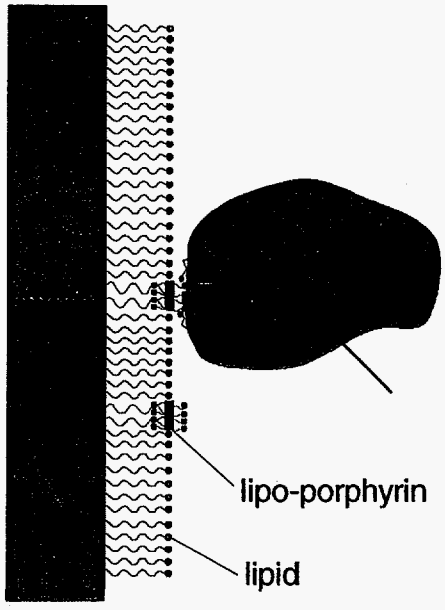

Figure 7b. *A simplified biosensor design allowed by the new lipoporphyrin. Embeded fullerene is not necessary due to the short distance over which the electrons must travel to the electrode surface.*

The synthesis of the $Sn(Cl)_2$LipoP ($Sn(IV)Cl_2$**1**), was completed as anticipated, but we ran into difficulty in converting **1b** to **1a**. LipoP **1a** has the most promising molecular recognition features because of its negatively charged carboxylate groups and because both methylviologen and the "docking ring" of cytochrome *c* are positively charged. Nevertheless, the synthesis of the $Sn(Cl)_2$ derivative of LipoP **1b** has allowed us to demonstrate electron transfer between the LipoP

and one of the sensor target molecules (*vide infra*), thus demonstrating one of the functional properties of the molecular recognition molecule that is necessary for construction of a working biosensor.

7. Synthesize lipoporphyrins with improved molecular recognition sites.

We have taken two approaches to synthesize LipoPs (**1d**) with improved molecular recognition sites. The near term approach is to continue to synthesize LipoPs with a ring of negative charge at the periphery. We now know that this approach is valid since in the last year we have demonstrated the binding of such a porphyrin (uroporphryin) to cytochrome *c* (see below and *Inorg. Chem.* manuscript) in collaboration with workers at the University of Hawaii. This is one of the reasons we are focusing on the synthesis of LipoP **1d** rather than LipoP **1a**. We have had considerable difficulty in hydrolyzing the methyl ester groups of LipoP **1b** to obtain **1a** without also hydrolyzing the long chain hydrocarbons on the phenyl substituents. We also tried synthesizing the analog of **1b** with the benzyl ester which we thought might be hydrolyzed under milder conditions than the methyl ester. However, even with the benzyl ester we were not able to selectively hydrolyze just the pyrrole substituents leaving the hydrocarbon tails intact.

Selective hydrolysis of the ester is not a problem in converting LipoP **1c** to **1d**, which also results in the ring of negative charges necessary to cause the binding of cytochrome *c*. This is because the ester linkage to the phenyl substituents of LipoP **1b** has been replaced by the ether linkage in LipoP **1c**. We have synthesized the nickel derivative of LipoP **1c** in a quantity large enough for full characterization (*vide infra*). Subsequently, the synthesis of LipoP **1c** has been scaled-up, and we are currently converting the Br groups to the thiols. We will then hydrolyze

the esters to obtain **1d**. This will give us our final molecular recognition component for the biosensor.

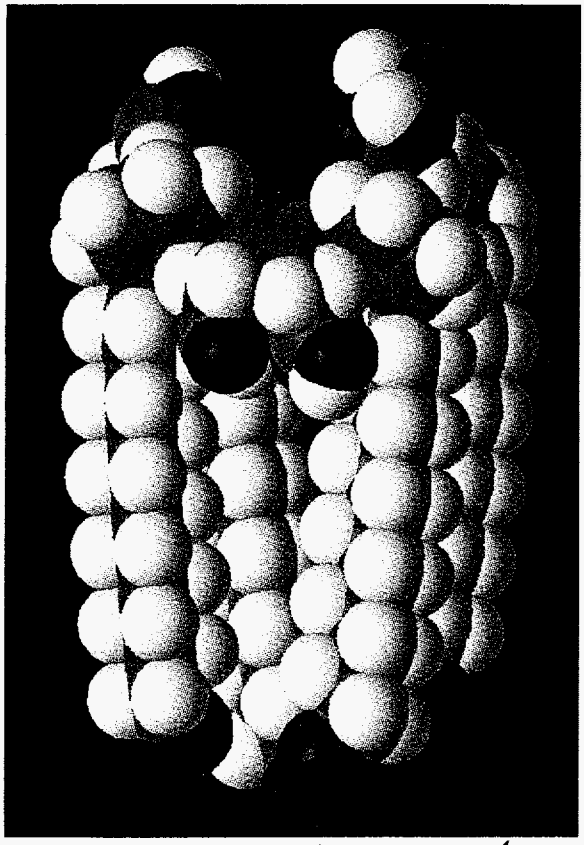

Figure 8. *Energy-optimized structure of* α *-Ni1c.*

Molecular modeling shows that the structures of the recognition sites of the LipoPs **1a** and **1d** are similar. However the *ortho* site at which the hydrocarbon tails are attached for LipoP **1d** gives a more favorable position of the tails for incorporation into films on the electrode surface. For LipoP **1c** and **1d** the tails are closely packed under the porphyrin head group as shown in Figure 8.

As a second longer range approach, we are investigating the synthesis of porphyrins with chiral molecular recognition sites. Because all proteins, indeed all amino acids (except glycine) of a protein, are chiral, it is desired to to be able to build a chiral recognition site to attain the highest possible selectivity for a specific protein. Thus, we have been pursuing the goal of synthesizing the analogs of LipoP **1d** in which the eight carboxylate groups are replaced by a specified enantiomer of a chiral substituent such as an amino acid. A new synthetic procedure, called the Suzuki reaction, is being used to accomplish this task. The procedure involves synthesizing the porphyrin in which the eight carboxylates are replaced by bromine atoms and these can subsequently be replaced by the boronic acid of a chirally pure substituent group. We have now demonstrated this is possible for non-chiral groups, and we are in the process of redoing this reaction with a chiral one.

Unfortunately, we ran out of time to convert **1c** to **1d**. Thus, we focused on studying the designed recognition, and photochemical properties using the $Sn(Cl)_2$ derivative of LipoP **1b** for one of the sensor target molecules. We carried the photoreaction in micelles and at water-organic interfaces to mimic the environment of electron-transfer between the porphyrin and target molecule in LB films. The result will demonstrate the functional properties of the molecular recognition molecule that is necessary for construction of a working biosensor.

8. Characterize lipoporphyrin-containing micelles.

Ternary systems were chosen to determine the electron transfer behavior of the designed tin lipoporphyrin (SnLipoP **1b**). Photoreaction rates were measured in micelles and at water-hexane interfaces to mimic the environment of electron transfer between aqueous solvent and the organic lipid phase of LB film. Two kinds of surfactant, cationic cetrimethylammonium bromide (CTAB) and anionic sodium dodecyl sulfate (SDS), are used to form micelles in order to determine the effect of surfactant charges on the electron transfer process. For comparison, electron transfer reactions photosensitized by two other porphyrins (shown in Figure **1f** and **1g**), the water-soluble tin protoporphyrin IX (SnPP, **1f**) and water-insoluble tin octaethylporphyrin (SnOEP, **1g**), were also studied in water, micelles, and/or at water/hexane interfaces. To understand the photochemical

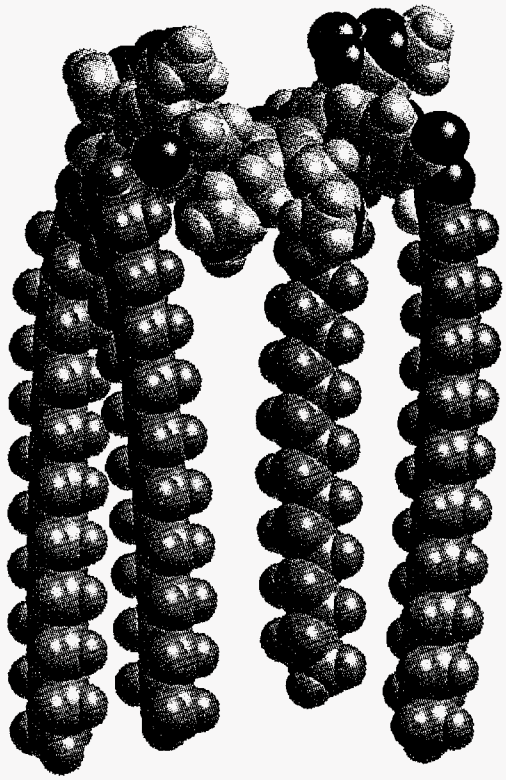

Figure 9. *Energy-optimized structure of Sn **1a**.*

properties of the Sn lipoporphyrin, it is necessary to know the locations of these porphyrins in the reaction systems, which is determined by their structural properties.

Figure 9 gives the energy optimized structure of SnLipoP. This lipoporphyrin consists of a porphyrin head group and four long alkane tails. The porphyrin head group is highly nonplanar because of the steric constraints of twelve bulky peripheral substituents which prevent the formation of porphyrin π–π aggregation. The eight carboxylate groups make the head group highly hydrophilic. When the porphyrin-hexane solution is added to the top of water, a layer of porphyrin will form at the hexane/water, with the porphyrin head group laying flat toward the water phase and the four hydrophobic tails in and toward the hexane phase. When the porphyrin is dissolved in micelles, the porphyrin head group will locate at the surface of micelles with the four tails inside the micelle as illustrated in Figure 10.

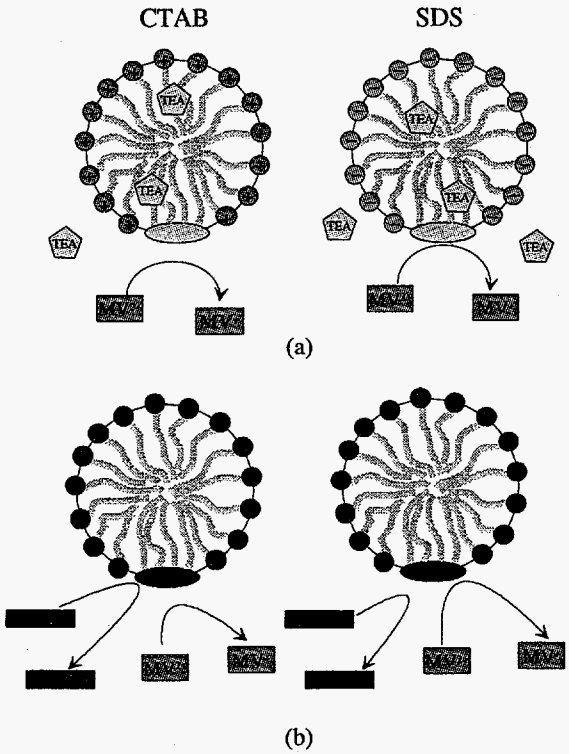

Figure 10. *Comparisons of the photoreaction sensitized by SnLipoP in CTAB (left panel) and SDS (right panel) micelles with TEA (a) and EDTA (b) as electron donor.*

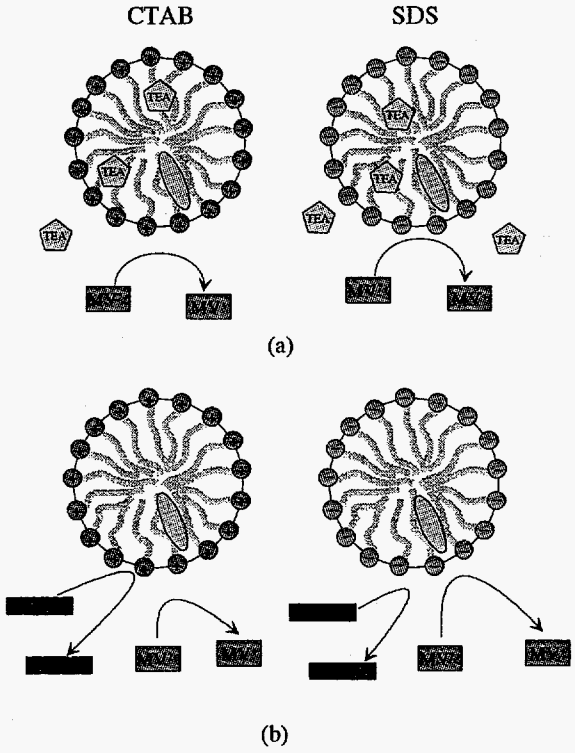

Figure 11. Comparisons of the photoreaction sensitized by SnOEP in CTAB (left panel) and SDS (right panel) micelles with TEA (a) and EDTA (b) as electron donor.

SnOEP and SnPP have an almost planar macrocycle which make them easily form π–π aggregation. These two porphyrin have very different hydrophilicity. SnOEP is totally hydrophobic. It can only be dissolved in hexane but not in water. When dissolved in aqueous micellar solutions, SnOEP molecule will locate inside the micelle as illustrated in Figure 11. These hydrophobic solvent environments prevent SnOEP from forming π–π aggregates.

SnPP is hydrophilic because of the two carboxylate groups which make the porphyrin water soluble. The porphyrin can form π–π aggregates in aqueous solution. The aggregation properties is highly PH-dependent. Figure 12 shows the titrated UV-visible absorption spectra of SnPP in water (middle panel) along with the corresponding spectra in CTAB micelles (top panel) and in SDS micelles (bottom panel). At high PH values in water, the Soret band is narrow, indicating the porphyrin is not aggregated (monomeric). The porphyrin is 6-coordinated with hydroxides. The strong axial ligation of hydroxides blocks the formation of π–π aggregation. As the pH decreases with titration, the Soret band becomes broader and a new peak appears at blue side at pH~6, indicating the hydroxide ligands has changed into water molecule. At the same time, a long-wavelength tail appears at the red side of the Soret band and extends to over 500 nm, indicating π–π aggregation caused by exciton

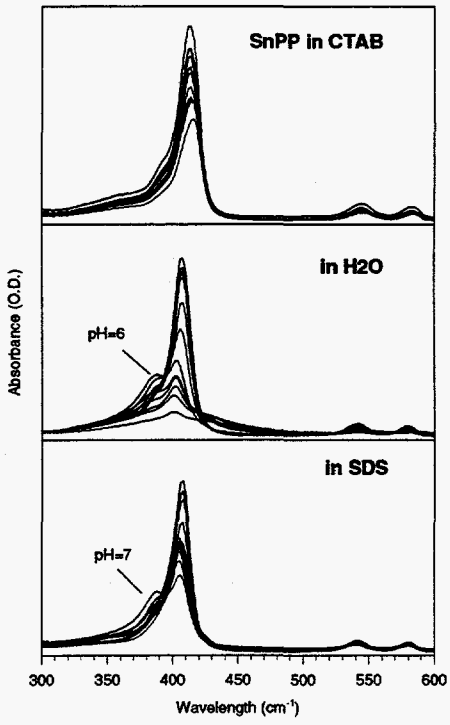

Figure 12. *UV-visible absorption spectra of SnPP in water (middle), CTAB micelles (top), and in SDS micelles (bottom) at different pH values by titrating the alkaline with HCl acid.*

coupling. The weak axial ligation of water molecules is not strong enough to block the π–π aggregation. Further lowering the pH, the new peaks gradually disappears and the long-wavelength red tails intensifies. The weak ligated water molecules turn to unligated protons (H_3O^+) and, hence, the aggregation increases.

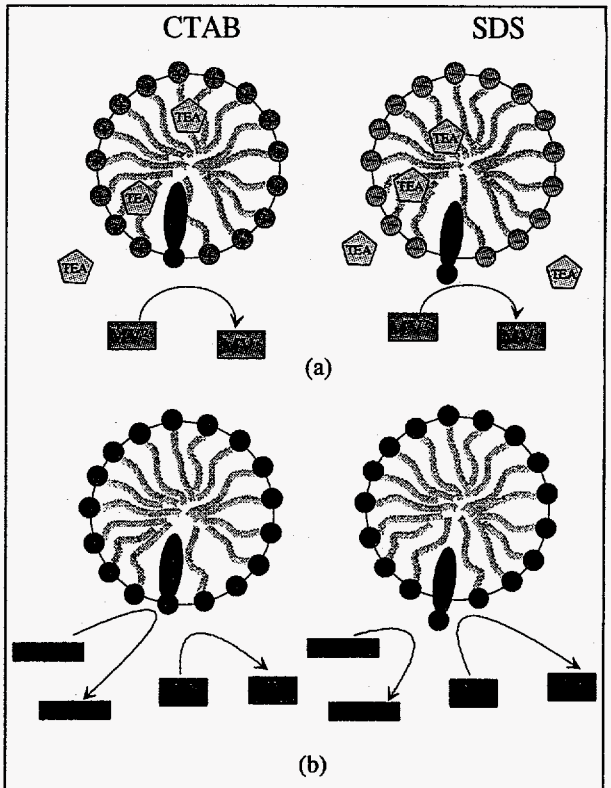

Figure 13. Comparisons of the photoreaction sensitized by SnPP in CTAB (left panel) and SDS (right panel) micelles with TEA (a) and EDTA (b) as electron donor

In the structure of SnPP, the two hydrophilic carboxylate groups are on one side and the rest of molecule including the porphyrin macrocycle is hydrophobic. Thus, when dissolved in a micellar solution, the hydrophilic macrocycle will inset into the hydrophobic phase of the surfactant tails of micelles, leaving the two carboxylate groups at the surface outside of the micelles. The insertion of the macrocycle into hydrophobic environment prevents the porphyrin from π–π aggregating. This is evidenced by the lack of the long-wavelength red tails in the absorption spectra of its micellar solutions shown in Figure 13. From Figure 13, we can also see that the degree of the macrocycle insertion is affected by the surfactant charges. The additional water-ligated absorption peak for SnPP in SDS micelles, whose maximum occurs at pH 7, indicates that the central metal, tin, of the porphyrin macrocycle is accessible by water molecules. In contrast, the lack of additional water-ligated absorption peak for SnPP in CTAB micelles indicates the inaccessibility of the central metal to water. Thus, almost the whole macrocycle of SnPP is inserted into the hydrophobic environment

in CTAB micelles, whereas in SDS micelles only half of the macrocycle, at the most, is inserted into the hydrophobic environment. This differences is illustrated in Figure 13. This is understandable in terms of effect of surfactant charges. The positively charged head group of CTAB surfactant molecule attracts the negatively charged carboxylate groups in the porphyrin substituents, resulting in the location of the carboxylate groups at the surface of the micelle and, hence, the insertion of the whole macrcocycle into the hydrophobic environment of the micelle. On the other hand, the negatively charged head group of the SDS surfactant molecule repels the negatively charged carboxylate groups in the porphyrin substituents, putting the carboxylate groups away from the micellar surface and, thus, leading to the smaller degree of the macrocycle insertion into the hydrophobic environment of the micelle.

9. Investigate photoelectrochemical properties of films containing lipoporphyrins.

We have demonstrated photochemical reduction of paraquat at monolayers and at micellar surfaces containing $Sn(OH)_2$LipoP **1b**. This was crucial for coupling the protein or herbicide binding event to the formation of an electrical current that can be measured to indicate binding and thus detection. This was accomplished by replacing the electrode, which in the completed biosensor assembly will provide electrons to reduce the excited state of the porphyrin, by a chemical electron donor. Triethanolamine (TEA) or ethylenediaminetetraacetic acid (EDTA) served as a sacrificial electron donor to reduce the Sn porphyrin in its triplet electronic state to the porphyrin radical anion. The Sn-porphyrin anion is long lived and ultimately transfers its extra electron to colorless paraquat (MV^{2+}) to form the deep blue paraquat radical anion ($MV^{\cdot}$). Formation of the reduced paraquat can be detected by eye and UV-visible absoption spectrophotometer in micellar solutions. We also detected reduced paraquat formation when light

was shined on the interface between an aqueous and organic phases. The kinetic behavior of photosensitized electron-transfer at water-organic solvent interfaces was found to be different from that in a macroscopically homogeneous solution (water and micelles). This difference is quantitatively accounted for by the steady-state kinetic treatment of a reaction mechanism, which involves the reductive primary electron transfer process of tin porphyrin, with a optical-shielding. The mechanism well explains distribution effects of porphyrin and electron-donor and the effects of surfactant charges.

Electron-Transport Kinetics. Methylviologen cation radical MV^{+}, the product of the photoreaction, is stable under our experimental conditions. Figure 14 shows the UV-visible absorption spectra of MV^{+} for photoreduction of methylviogen with TEA as the donor when sensitized by SnLipoP in a hexane/water two phase system. The MV^{+} concentration is measured in the water phase at different times. The methylviologen cation radical exhibits a characteristic absorption at 395 nm and at 602 nm. The 602 nm absorption is used for monitoring the production of MV^{+}. Different kinetic behaviors are observed for photoreaction of the ternary systems in macroscopically homogeneous solutions (micellar and aqueous solutions) and in the water-organic solvent systems. A logarithmic-like relationship between the MV^{+} concentration and irradiation time is observed for photoreaction in a macroscopically homogeneous solution in which the reactants, photosensitizer, and products are in the same

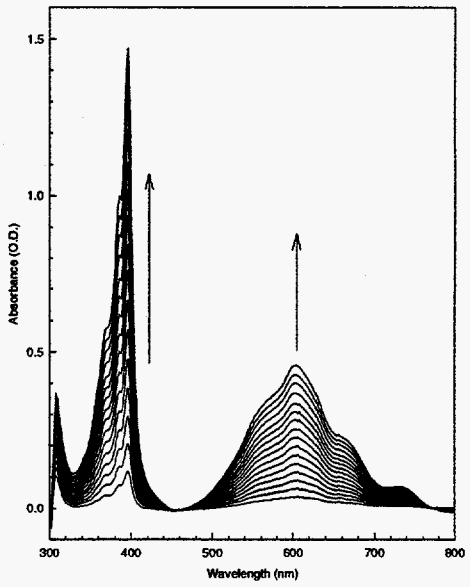

Figure 14. *UV-visible absorption spectra of* MV^{+} *from photoreduction of methyl viologen by TEA sensitized by SnLipoP at hexane/water interface taken at the water phase at different time.*

phase. For example, Figure 15 shows the logarithmic -like dependence of $[MV^{+}]$ on the irradiation time for the EDTA-SnPP-MV^{2+} ternary system in aqueous solution at pH = 12. On the other hand, for ternary systems involving a water-organic solvent interface, a linear relationship between the MV^{+} concentration and irradiation time is observed. Figure 16 shows the linear dependence of photoreduction of MV^{+} when sensitized by SnLipoP in the hexane/water system with TEA as the donor.

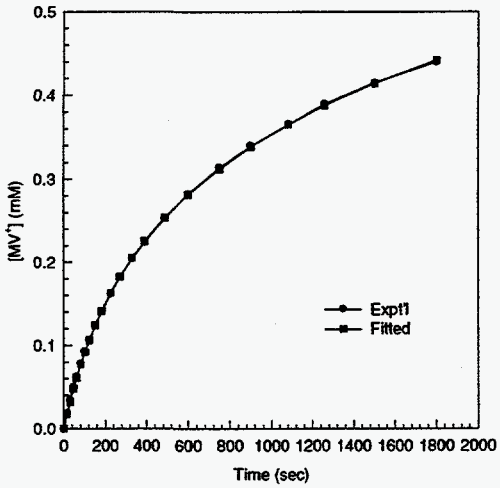

Figure 15. *The dependence of* MV^{+} *concentration on irradiation time (circles) for photo-reduction of methyl viologenby EDTA sensitized by SnPP in water, and the curve fitting results (squares) with equation* $[MV^{+}] = a\ln(1+bt)$.

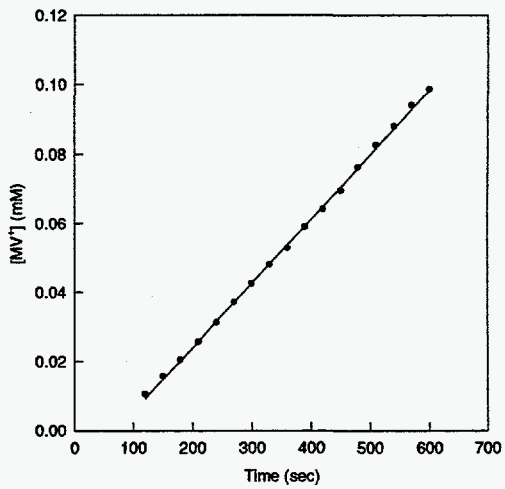

Figure 16. *The linear dependence of* MV^{+} *concentration on irradiation time for photo-reduction of methyl viologen by TEA sensitized by by SnLipoP at hexane/water interface.*

To explain this different kinetic behavior, a photoreaction kinetic mechanism is proposed based on a primary reductive electron-transfer process. Because the redox potential of tin porphyrins (SnP/SnP^{-}) is lower than that of methylviologen (MV^{2+}/MV^{+}) and the redox potential of excited tin porphyrins (SnP^{*}/SnP^{-}) is higher than that of methylviologen but lower than that of electron donor ($EDTA^{+}$/EDTA, TEA^{+}/TEA), the tin porphyrin in the excited state can accept an electron from the electron donor and transport the electron to the electron acceptor methyl-

viologen. A kinetic mechanism is proposed which also takes into consideration the fact that methylviologen cation radical also absorbs light and that the porphyrin in the excited state and methylviologen cation radical can return to their ground states by colliding with solvent molecules.

$$P + h\nu \xrightarrow{k_1} P^* \quad (1)$$

$$P^* + EDTA \xrightarrow{k_2} P^{-} + EDTA^{\cdot+} \quad (2)$$

$$P^{-} + MV^{2+} \xrightarrow{k_3} P + MV^{\cdot+} \quad (3)$$

$$P^* + S \xrightarrow{k_4} P + S \quad (4)$$

$$MV^{\cdot+} + h\nu \xrightarrow{k_5} MV^{\cdot+*} \quad (5)$$

$$MV^{\cdot+*} + S \xrightarrow{k_6} MV^{\cdot+} + S \quad (6)$$

Here we use steady-state theory to treat the reactions. At steady state, the reaction rates for all of the intermediates are equal to zero. The intermediates are P^*, P^{-}, and $MV^{\cdot+*}$; thus, we have,

$$\frac{d[P^*]}{dt} = k_1[P]I - k_2[P^*][EDTA] - k_4[P^*][S] = 0 \quad (7)$$

$$\frac{d[P^{-}]}{dt} = k_2[P^*][EDTA] - k_3[P^{-}][MV^{2+}] = 0 \quad (8)$$

$$\frac{d[MV^{\cdot+*}]}{dt} = k_5[MV^{\cdot+}]I - k_6[MV^{\cdot+*}][S] = 0 \quad (9)$$

The reaction rate in term of $MV^{\cdot+}$ production is,

$$\frac{d[MV^{\cdot+}]}{dt} = k_3[P^{-}][MV^{2+}] - k_5[MV^{\cdot+}]I + k_6[MV^{\cdot+*}][S] \quad (10)$$

After substituting the concentrations for the intermediates obtained from equations (7), (8) and (9) into (10), the reaction rate for MV^{+} production is given by,

$$\frac{d[MV^{+}]}{dt} = \frac{k_1 k_2 I[P][EDTA]}{k_2[EDTA] + k_4[S]}. \qquad (11)$$

The solvent concentration is constant. Experimentally, the electron donor is in great excess and its concentration is virtually a constant. Under these conditions the reaction rate is given by,

$$\frac{d[MV^{+}]}{dt} = K[P]I, \qquad (12)$$

where $K = \frac{k_1 k_2 [EDTA]}{k_2[EDTA] + k_4[S]}$. (13)

In the ternary reaction system, the porphyrin concentration is a constant. When the incident light intensity on "porphyrin molecules" I remains unchanged, after integration, equation (12) will becomes,

$$[MV^{+}] = K[P]It, \qquad (14)$$

and the MV^{+} concentration will depend linearly on irradiation time.

The incident light intensity on "porphyrin molecules" I is not a constant for the macroscopically homogeneous solutions in which the porphyrin and produced methylviologen cation radical are in the same phase. The blue colored MV^{+} will also absorb light, producing *shielding* effect on porphyrin absorption. The light intensity after passing l cm thick solution becomes

$$I = I_0 e^{-\varepsilon_p l[p]} e^{-\varepsilon_{mv^+} l[mv^+]} \qquad (15)$$

Assuming that the photoreaction cell is thin, we can use the light intensity at the half width ($l=\frac{1}{2}L$) of the cell as the average intensity over the cell width L. Then, after substituting equation (15) into (12), we get

$$\frac{d[\mathrm{MV}^{+}]}{dt} = k[\mathrm{P}]I_0 e^{-\varepsilon_{\mathrm{P}} l[\mathrm{P}]} e^{-\varepsilon_{\mathrm{MV}^{+}} l[\mathrm{MV}^{+}]} \tag{16}$$

When t=0, i.e. $[\mathrm{MV}^{+}]$=0, the initial reaction rate is

$$\left(\frac{d[\mathrm{MV}^{+}]}{dt}\right)_0 = kI_0[\mathrm{P}]e^{-\varepsilon_{\mathrm{P}} l[\mathrm{P}]} \tag{17}$$

After integration over t, the equation (16) becomes

$$[\mathrm{MV}^{+}] = a\ln(1+bt) \tag{18}$$

where $a=\frac{1}{\varepsilon_{\mathrm{MV}^{+}} l}$ and $b=\varepsilon_{\mathrm{MV}^{+}} lkI_0[\mathrm{P}]e^{-\varepsilon_{\mathrm{P}} l[\mathrm{P}]}$. The relationship between MV^{+} concentration and irradiation time is nonlinear. MV^{+} concentration has a logarithmic-like but not logarithmic dependence on irradiation time.

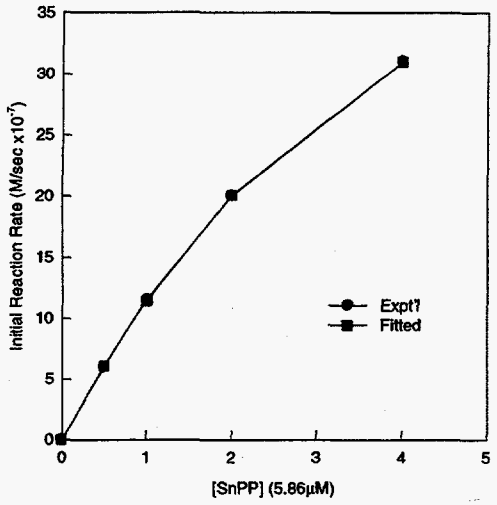

Figure 17. The dependence of initial photoreaction rate on porphyrin (SnPP) concentration [P] in water and the curve fitting results with equation $r_0 = a[\mathrm{P}]e^{-\varepsilon_P l[\mathrm{P}]}$.

This mechanism and kinetics treatment can quantitatively explain the observed different kinetic behaviors for photoreaction of the ternary systems in macroscopically homogeneous solutions (micellar and aqueous solutions) and at the water-organic solvent interfaces. For photoreaction of the ternary systems at the water-organic solvent interfaces, water insoluble porphyrin (SnLipoP, SnOEP) and water soluble MV^{+} are at different phases. MV^{+} in water does not *shield* porphyrin in hexane. The light intensity irradiated on porphyrin does not change with reaction time. Thus, the MV^{+} concentration will depend linearly on irradiation time (equation (14) and Figure 16). The reaction rate is a constant. In a macroscopically homogeneous solution (water, micelles), however, MV^{+} is in the same phase with porphyrin and will produce a shielding effect on it (equation (18) and Figure 15). Using equation (18) to fit the experimental data shown in Figure 15, we get an (almost) exact fitting, confirming the validity of the mechanism and kinetic treatment. The fitting curve is also shown in Figure 15. The absorbancy index of MV^{+}, $\varepsilon_{MV^{+}}$, can also be obtained from fitting a in equation (18). The obtained $\varepsilon_{MV^{+}}$ from fitting (9,700 $M^{-1}cm^{-1}$ at 602 nm) agrees well with the experimental value (1.0 x 10^4 $M^{-1}cm^{-1}$)[13] used to calculate MV^{+} concentration. Thus, the commonly observed nonlinear dependence of MV^{+} concentration on irradiation time is not due to " the reaction itself" but due to the shielding effect of MV^{+} on porphyrin.

Figure 17 shows the dependence of initial photoreaction rate on porphyrin concentration for the EDTA-SnPP-MV^{2+} ternary system in aqueous solution at PH=12. The validity of the mechanism and kinetic treatment is further solidified by the (almost) exact fitting of the experimental data with equation (17). The fitting curve is also shown in Figure 17. Further, the absorbancy index of SnPP, ε_P, obtained from fitting (1.48 x 10^4 $M^{-1}cm^{-1}$) is also in accordance with the our experimental value (1.58 x 10^4 $M^{-1}cm^{-1}$).

This mechanism can also be used to explain the distribution effects of electron donor and electron acceptor at different phases, the distribution effects of porphyrin at different phases, and the effects of surfactant charges (Table 3).

Effect of Electron-Donor Distribution. Comparing the initial photoreaction rate using TEA as electron donor with that using EDTA as electron donor under the same reaction conditions, we can find that the reaction is slower with TEA than with EDTA in water, but faster with TEA that with EDTA in micelles and at hexane/water interfaces. This can be understood from the reaction mechanism and their distribution differences in the ternary reaction systems.

Microscopically, the solution is homogeneous in water. Electron donor and acceptor molecules can easily access the photosensitizer from all the directions. The slower photoreaction with TEA than with EDTA in water may reflect the nature of the reaction. The micellar solution and the hexane/water interface reaction system are either microscopically or macroscopically homogeneous. There exist micro- or macro-hydrophobic and hydrophilic environments. The distribution of electron donor in these environments will influence its availability for reaction and hence the reaction rate. This can be best illustrated using the hexane/water reaction system shown in Figure 18. For the hexane/water interface reaction system, the water-insoluble photosensitizer porphyrin (SnLipoP, SnOEP) is in hexane and the water soluble electron acceptor methylviologen

is in water. When electron-donor (such as TEA) can be in hexane, the same environment as the photosensitizer (porphyrin), there is only one step interface reaction (step 3). The first two steps, excitation of porphyrin and production of porphyrin anion, are fast since electron transfer occurs in the same phase. In the third step, the porphyrin anion in hexane needs to deliver the electron to methylviologen in water. Electron transfer between two phases slow down the reaction but there are still considerable chances for reaction. When electron donor (such as EDTA) are not soluble in hexane and thus are not in the same of the porphyrin, the two steps of electron transfer, EDTA to the porphyrin and porphyrin anion to methyl viologen, both occurs at the interface between two different phases. This results in very few chances to get methyl viologen cation radical. Consequently, there is almost no reaction when EDTA is used as the electron donor at hexane/water interfaces. The faster reaction sensitized by SnLipop than by SnOEP at hexane/water interfaces may due to the hydrophilic property of the SnLipoP head group which causes the formation of the lipoporphyrin monolayer at the interface in contrast to SnOEP as discussed earlier.

The distribution of electron donors also affects the photoreaction rate in micelles. Since TEA can be solvateded both inside and outside of micelles whereas EDTA can only be solvateded outside of micelles, the reaction rates in micelles with TEA as electron donor are generally bigger that those with EDTA (Table3). However, the influence of electron donor distribution on reaction in micelles is not so big as at hexane/water interfaces because micellar solutions are macroscopically homogeneous.

Effects of Micelle and Porphyrin Nonplanarity. There have been a lot of studies on the effects of micelles on photoreactions sensitized by porphyrins. Their results show that micelles can promote the production of MV^{+} by preventing the formation of tight porphyrin-methylviologen complex and providing a barrier to back electron transfer. Our results show that this is not always necessarily true for any case. It depends on the structural properties of porphyrin. The nonplanarity of the porphyrin influences back electron transfer. For planar porphyrins or porphyrins with low degree of nonplanarity such as SnPP and SnOEP in the present study, tight π–π porphyrin-methylviologen complex can be formed, leading to strong back electron transfer. Putting the porphyrin in micelles prevents the close approach of methylviologen to the porphyrin and, hence, achieves an efficient charge separation for suppressing back electron transfer. When the porphyrin is highly substituted, which causes the porphyrin to become highly nonplanar in order to release the energy of steric interactions of the substituents, the high degree of nonplanarity of the macrocycle and the steric constraints prevent the formation of the tight π–π porphyrin-methylviologen complex, providing sufficient charge separation to reduce back electron transfer. In the present case, the twelve bulky peripheral carboxylate substituents of SnLipoP cause the porphyrin head group to be highly nonplanar, resulting in a saddle shape of the

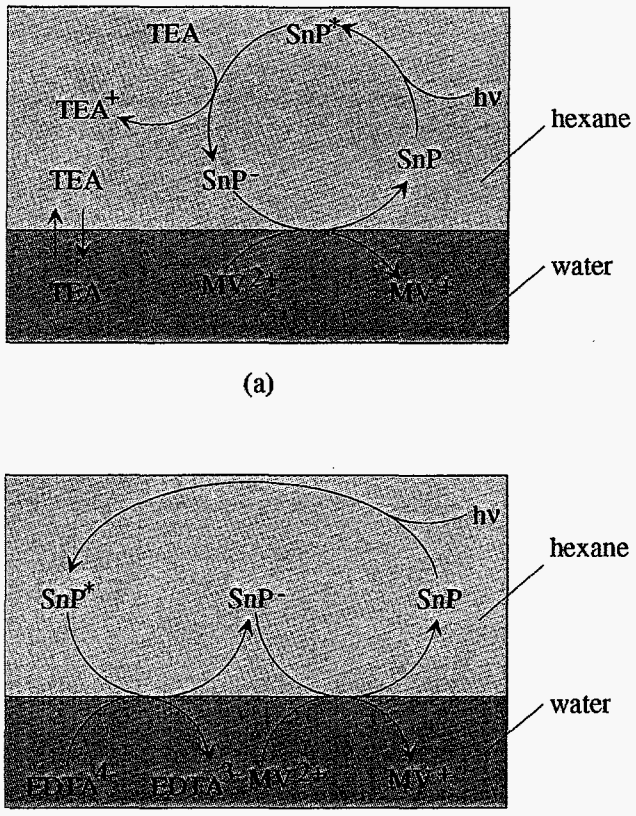

Figure 18. *Comparisons of the photoreaction sensitized by SnLipoP at hexane/water interface with TEA (a) and EDTA (b) as electron donor.*

macrocyle. The saddle shape does not allow methyl viologen to stack *flat* against the porphyrin macrocycle, which leads to the formation of tight co-planar (II) π–π porphyrin-methylviologen complex. Such a porphyrin does not need to be put in micelles to suppress the back electron transfer and promote the reaction rate. Thus, the reaction rate sensitized by SnLipoP in micelles does not improve much and is even worse when using TEA as an electron donor (Table 3).

Table 3. *The initial reaction rates of MV^{2+} reduction photosensitized by tin porphyrins in water, micelles and at water/organic solvent interfaces*

Porphyrin	Solution Type	Initial Rate (10^{-7}M/sec) with TEA	Initial Rate (10^{-7} M/sec) with EDTA
SnLipoP	hexanes/H_2O interface [a]	2.44	very small
	CTAB micelles[b]	0.65	0.41
	SDS micelles [b]	1.76	0.59
SnOEP	benzene/H_2O interface [c]	1.05	very small
	CTAB micelles[c]	10.7	9.56
	SDS micelles [c]	25.8	11.7
SnPP	H2O (pH=12) [d]	14.4	19.8
	CTAB micelles[d]	22.0	20.7
	SDS micelles [d]	20.9	15.4

Reaction conditions:
[a] *$[MV^{2+}] = 0.020$ M, [SnLipoP] = ~ 1 μ M, [TEA] = [EDTA] = 0.40M.*
[b] *$[MV^{2+}] = 0.040$ M, [SnLipoP] = ~ 1 μ M, [TEA] = [EDTA] = 0.80M.*
[c] *$[MV^{2+}] = 0.020$ M, [SnOEP] = 7.0 μ M, [TEA] = [EDTA] = 0.40M.*
[d] *$[MV^{2+}] = 0.020$ M, [SnPP] = 11.8 μ M, [TEA] = [EDTA] = 0.40M.*

Effect of Surfactant Charges. When the photoreaction is carried out in micelles, surfactant charges have a significant influence on the reaction. Thus, we observed different initial reaction rates in CTAB and SDS micelles under the same conditions. The specific difference for each shown in Table 1 can be explained by combining the effect of surfactant charges with the charge and location properties of electron donor porphyrins in micelles.

TEA is neutral and distributes both outside and inside micelles. When using TEA as electron donor, surfactant charges only influence the reduction of methylviologen, step 3 in the reaction mechanism shown earlier. When the porphyrin is uncharged (such as SnLipoP and

SnOEP), the positively charged micelle surface repels the positively charged methyl viologen, hindering its approach to the porphyrin at the surface and thus slowing down the reaction. In contrast, negatively charged micelle surface attracts the positively charged methyl viologen, favoring its approach to the surface porphyrin and hence accelerating the reaction. Thus the photoreaction sensitized by SnLipoP and SnOEP is faster in SDS micelles than in CTAB micelles. This is illustrated in Figure 10a and 11a. The photoreaction rates sensitized by SnPP in CTAB and SDS micelles (with TEA as electron donor) are almost the same (Table 3). This results from two opposite factors: the effect of surfactant charges causes the reaction faster in SDS micelles than in CTAB micelles; the other factor is micellar environment. As discussed earlier, it promotes the reaction sensitized by SnPP in both CTAB and SDS micelles. However, this promotion effect is smaller for reaction in SDS micelle than in CTAB micelle because SnPP is more out of micelle in SDS micelle than in CTAB micelle (show in Figure 13a) due to electrostatic interaction between the surfactant charges and negatively charged carboxylate groups in the porphyrin substituents as discussed above.

EDTA is an anion and can only be solvated in water outside of micelles. Thus negatively charged surface of micelles will repel it from approaching the surface, slowing down the production of porphyrin anion (step 2 in the mechanism); and positively charged surface of micelles will attract it to the surface, speeding up the reaction of step 2. Since the charges of EDTA and methyl viologen are just opposite, a (negatively or positively) charged surface of a micelle will influence the reaction rates of step 2 and step 3 in the mechanism in an opposite way (as illustrated in Figure 10b, 11b and 12b). This results in diminishing the difference of the overall reaction rate in negatively charged and positively charged micelles. So the observed initial reaction rate with EDTA as electron donor does not differ not in CTAB and SDS micelles

sensitized by SnLipoP or SnOEP (Table 3). It is also noted that the observed initial rate sensitized by SnPP is considerably slower in SDS micelles than in CTAB micelles. This larger difference is due to the different location of the porphyrin in these micelles. Being more outside of the porphyrin in SDS micelles leads to the promotion of the reaction by the micellar environment to a lesser degree in SDS micelles than in CTAB micelles.

In conclusion, the designed lipoporphyrin SnLipoP shows the desired electron transfer properties at water-organic solvent interfaces, making it very promising to be used as recognition site for chemical- and bio-sensor applications.

DISTRIBUTION:

1	MS-1425	M. W. Scott (1307)
1	MS-1425	S. J. Martin (1315)
1	MS-0958	C. Adkins (1472)
1	MS-1079	A. D. Romig (1300)
1	MS-1435	H. J. Saxton (1800)
1	MS-1434	G. E. Pike (1802)
1	MS-1349	R. E. Loehman (1808)
1	MS-0333	A. J. Hurd (1841)
1	MS-1435	M. J. Cieslak (1860)
3	MS-1349	J. Cesarano, III (1831)
1	MS-1349	C. J. Brinker (1831)
1	MS-1349	W. F. Hammetter (1846)
1	MS-0188	D. L. Chavez (4523)
1	MS-0724	J. B. Woodard (6000)
1	MS-0702	D. E. Arvizu (6200)
1	MS-0710	A. P. Sylwester (6210)
5	MS-0710	J. A. Shelnutt (6210)
1	MS-0710	C. Kyle (6210)
1	MS-0710	X.-Z. Song (6210)
1	MS-0710	J.-G. Ma (6210)
1	MS-0710	S.-L. Jia (6210)
1	MS-0710	G. N. Ryba (6210)
1	MS-0710	T. M. Nenoff (6210)
1	MS-9214	L. M. Napolitano (8117)
1	MS-9405	J. M. Hruby (8230)
1	MS-9161	W. G. Wolfer (8717)
1	MS-1111	G. Heffelfinger (9225)
1	MS-1111	J. D. Hobbs (9225)
1	MS-9018	Central Technical Files (8940-2)
5	MS-0899	Technical Library (4414)
2	MS-0619	Review & Approval Desk (12690) For DOE/OSTI